Optimized Quadruple Phase-Shift Modulation of 3/2LNPC-DAB Converters for Full-Power-Range Soft-Switching and Minimum Peak Current

Jiayun Liu, Cheng Tang, Jiayu Hu, Qianming Xu, *Member, IEEE*, Peng Guo, *Member, IEEE*, Guanqing Zhou, Xiangpeng Liu, and Zhikang Shuai, *Senior Member, IEEE*

***Abstract*—The symmetrical phase-shift modulation of the three-to-two-level neutral-point-clamped (NPC) dual-active-bridge (DAB) dc–dc converter has more controllable control variables than that of the conventional two-level DAB converter. The increase in control variables leads to an increase in the number of operating modes and inequality constraints, significantly complicating the modulation optimization process. To enhance the efficiency of the converter, this article proposes an optimized quadruple phase-shift (OQPS) modulation considering both conduction losses and switching losses. Five effective operating modes that have the potential to achieve zero-voltage-switching (ZVS) for all switching devices are screened based on the ZVS inequality constraints. The inductor peak current is used as an optimization objective to minimize the conduction losses while satisfying the ZVS inequality constraints. The boundary of the feasible region satisfied by the optimal solution is derived by numerical optimization. Based on this, an improved Lagrange function and Karush–Kuhn–Tucker conditions are proposed to solve the analytical solution of OQPS modulation. Finally, the proposed OQPS modulation is applied to a 1.6-kW prototype to verify the improvement of efficiency. The designed prototype can achieve 96.9% peak efficiency at 300-V input and 150-V output voltages. Compared with previous modulations, the proposed OQPS modulation can achieve the highest efficiency in the full power range.**

***Index Terms*—Multilevel dual-active-bridge (DAB) converters, optimal modulation, peak current, quadruple phase shift (QPS), soft switching.**

I. Introduction

THE dual-active-bridge (DAB) converters are widely employed in applications, such as solid-state transformers, dc microgrids, and electric vehicles, due to their soft-switching capability, bidirectional power flow, and inherent electrical isolation [1], [2], [3]. In conventional two-level DAB converters, each switching device is subjected to the full port voltage [4]. To adapt to high-voltage input applications, the multilevel topology [5], [6] and the input-series output-parallel (ISOP) structure [7], [8] are commonly adopted to enhance the voltage withstand capability at the input side. Compared to the ISOP structure, the three-to-two-level neutral-point-clamped dual-active-bridge (3/2LNPC-DAB) converter, shown in Fig. 1, eliminates the issue of power imbalance among submodules, while also reducing the number of switching devices on the low-voltage side and high-frequency transformers [9]. Although the previous modulations of the conventional two-level DAB converter can be adapted to the 3/2LNPC-DAB converter, they fail to achieve optimal efficiency. Hence, to improve the converter efficiency, modulation optimization of the 3/2LNPC-DAB converter should be prioritized.

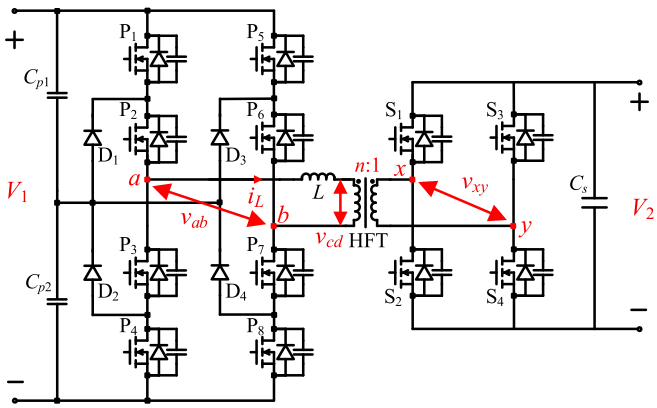

Fig. 1. Topology of the 3/2LNPC-DAB converter.

Symmetrical phase-shift modulation is widely used in DAB converters for transferred power control [10], [11]. Based on the number of control variables, symmetrical phase-shift modulation can be sequentially classified as single-phase-shift (SPS) modulation [12], double-phase-shift (DPS) modulation [13], triple-phase-shift (TPS) modulation [14], [15], and quadruple-phase-shift (QPS) modulation [16], [17]. Therein, the SPS modulation has only one control variable, which is uniquely determined by the transferred power. For other

Received 13 July 2025; revised 15 November 2025; accepted 2 January 2026. Date of publication 12 January 2026; date of current version 20 March 2026. This work was supported in part by the National Key Research and Development Program of China under Grant 2024YFB2409300 and in part by the Scientific Research Innovation Capability Support Project for Young Faculty under Grant ZYGXQNJSKYCXNLZCXM-D4. Recommended for publication by Associate Editor N. Tan. *(Corresponding author: Cheng Tang.)*

Jiayun Liu, Cheng Tang, Qianming Xu, Peng Guo, Guanqing Zhou, Xiangpeng Liu, and Zhikang Shuai are with the State Key Laboratory of High-Efficiency and High-Quality Conversion for Electric Power, Hunan University, Changsha 410082, China (e-mail: ljy666@hnu.edu.cn; tc_byron@hnu.edu.cn; xqm@hnu.edu.cn; pengguo92@hnu.edu.cn; zhougq1998@hnu.edu.cn; liuxiangpeng@hnu.edu.cn; szk@hnu.edu.cn).

Jiayu Hu is with the Sungrow Power Supply Company, Hefei 230000, China (e-mail: hujiayu@hnu.edu.cn).

Color versions of one or more figures in this article are available at https://doi.org/10.1109/TPEL.2026.3651518.

Digital Object Identifier 10.1109/TPEL.2026.3651518

multiple phase-shift modulations, extra control variables have the potential to widen the zero-voltage-switching (ZVS) range or reduce the inductor current to optimize the performance of the converter. The increase in the number of control variables leads to an increase in the number of operating modes and inequality constraints, thereby elevating the complexity of analyzing the modulation optimization process [18]. Meanwhile, the presentation of optimization results has also become more intricate. For example, in TPS modulation, the control variables in the analytical solution of modulation with current root mean square (rms) as the optimization objective can no longer be expressed directly in terms of transfer power and voltage conversion ratio ($k = V_1/nV_2$) [19]. For QPS modulation, an additional phase-shift control variable is introduced, which further increases the optimization complexity of the modulation.

Optimization methods for modulation strategies are divided into analytical solution [20], [21] and numerical solution [22], [23], [24]. Benefiting from the powerful computational capabilities of computers, numerical solution is often employed to obtain the optimized modulation more conveniently. Wang et al. [25] used the particle swarm algorithm to optimize the peak current of a 3/3LNPC-DAB converter. However, in the time domain, determining the objective function is challenging due to the numerous modes. To simplify the determination of the objective function, the research is based on DPS modulation. The advantage of the large number of control variables is not fully exploited. In [26], Find minimum of constrained nonlinear multivariable function (Fmincon) in MATLAB is applied to a half-bridge three-level neutral-point-clamped (NPC)-DAB converter to achieve ZVS and reduce the inductor current rms. However, the optimized modulation is based on TPS modulation and is not applicable to the full-bridge three-level NPC-DAB converter.

In the numerical solution, the optimization results need to be precalculated offline and stored in the microcontroller. Nevertheless, the microcontroller's limited memory restricts application to the operating conditions, where the voltage conversion ratio and the transferred power vary over a wide range. In contrast, the application of the analytic solution can be more flexible. The authors in [27] and [19] proposed analytical solutions for the TPS optimal modulation strategies with peak current and current rms as the optimization objectives, respectively. However, only the conduction loss of the converter is considered in these two optimized modulation strategies. In [28], a TPS-optimized modulation strategy is proposed combining ZVS realization and inductor current rms minimization. However, for QPS modulation, the further increase in the number of control variables elevates the complexity of solving the analytical solution. The authors in [29] and [30] analyzed QPS modulation by combining numerical optimization. Among them, Song et al. [29] proposed an analytical solution for the QPS-optimized modulation strategy with peak current as the optimization objective. In order to further improve the efficiency of the converter, Song et al. [30] considered the ZVS inequality constraint based on the previous research to lower the switching losses. However, the control variables in [29] are overconstrained, leading to less precise solutions at light loads. In [30], although the overconstraints on variables are resolved, the analysis and screening of the optimal operating modes is not comprehensive. Comparisons with previous optimization schemes in DAB converters are shown in Table I. In summary, the analytical solutions for TPS-optimized modulation are relatively mature, while those for QPS-optimized modulation have not been fully explored.

Soft switching is an unignorable advantage in DAB converters. To simultaneously reduce switching losses and conduction losses, this article proposes a multiobjective optimized quadruple phase-shift (OQPS) modulation that simultaneously achieves ZVS and inductor peak current minimization. The key innovations of this article are summarized as follows.

1) An analytical solution for QPS modulation to minimize the peak current of the 3/2LNPC-DAB converter under soft switching of all switching devices is proposed. This analytical solution is applicable across the entire voltage and power range, significantly improving the efficiency of 3/2LNPC-DAB converters under wide input/output voltage variations and light load conditions.
2) Five operating modes with the potential to achieve ZVS for all switching devices are screened. Based on numerical optimization, there are two such optimal modes for $0 < k < 1$, three for $1 < k < 2$, and two for $k > 2$.
3) The improved Lagrange function and Karush–Kuhn–Tucker (KKT) conditions are proposed to simplify solving the analytical solutions for OQPS modulation.

The rest of this article is organized as follows. The modulation model of the 3/2LNPC-DAB converter is developed, and the ZVS constraints are analyzed in Section II. In Section III, the optimal operating modes are screened based on the ZVS constraints. The transferred power expressions and inductor peak current expressions for each optimal operating mode are derived. The improved Lagrange function and KKT conditions are presented in Section IV. The boundary of the feasible region satisfied by the optimal solution can be derived by numerical optimization. Based on this, the analytical solution of the OQPS modulation can be derived by solving the improved Lagrange function and KKT conditions. The analysis of power loss is elaborated in detail in Section V. Section VI validates the effectiveness of the proposed OQPS modulation by experiments. Compared to previous advanced modulations, the proposed OQPS modulation still achieves a 2.1% efficiency improvement. Finally, Section VII concludes this article.

II. ZVS Analysis of the 3/2LNPC-DAB Converter

A. Basic Characteristics

The power transfer characteristics of the DAB converter can be decided by the inductor current. The inductor current variation depends on the midpoint voltage output of the full bridge on both sides, as shown in the following equation:

$$\frac{di_L(t)}{dt} = \frac{v_{ab}(t) - v_{cd}(t)}{L}. \tag{1}$$

The analytical expressions of the inductor current can be obtained according to the symmetry of the inductor current during the switching cycle in steady state. Furthermore,

TABLE I
COMPARISONS WITH PREVIOUS OPTIMIZATION SCHEMES IN DAB CONVERTERS

DAB converters	references	Number of DoFs	Solutions	Optimization Objectives	Optimization method	Modal analysis	Number of power stages
Two-level DAB	[27]	3	Analytical solution	Current stress	Differential extremum method	★★★	4
	[19]	3		RMS current	Global optimal condition (GOC) method	★★★	6
	[28]	3		rms current + ZVS	KKT method	★★★	6
3/3LNPC-DAB	[24]	5	Numerical solution	rms current	Frequency domain method	★	/
	[25]	2		rms current	Particle swarm optimization (PSO) method	★★★	/
Half-bridge 3/3LNPC-DAB	[26]	3		rms current + ZVS	Fmincon function method	★★★	/
2/3LNPC-DAB	[29]	4	Analytical solution	Current stress	Numerical optimization + KKT method	★	8
	[30]	4		Current stress + ZVS	Numerical optimization + KKT method	★★	10
3/2LNPC-DAB	this article	4		Current stress + ZVS	Numerical optimization + improved KKT method with low computational burden	★★★	13

For modal analysis, more ★ indicate more comprehensive modal analysis.

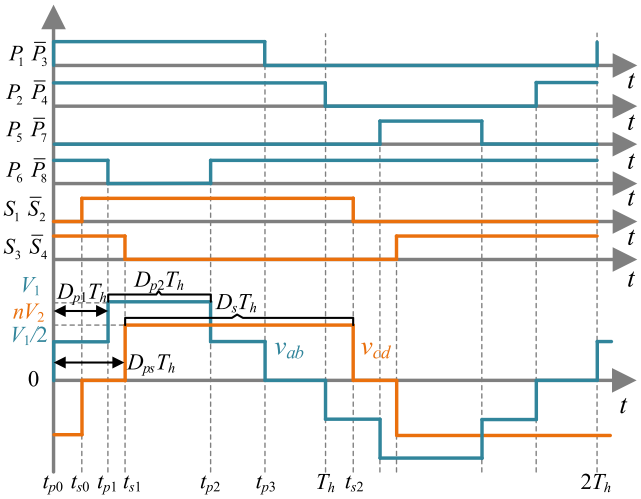

Fig. 2. Typical operating waveform of the 3/2LNPC-DAB converter.

the transferred power of the converter can be derived as follows:

$$P_{tr} = \frac{1}{T_h}\int_0^{T_h} v_{ab}(t)\, i_L(t)\, dt. \tag{2}$$

Fig. 2 presents a typical operating waveform of 3/2LNPC-DAB converters under the QPS modulation. The voltage v_{ab} has five levels $\pm V_1$, $\pm V_1/2$, and 0. The voltage v_{cd} has three levels $\pm nV_2$ and 0. For ease of description of the control variables, the $\pm V_1/2$ level is defined as the minor level of v_{ab} and the $\pm V_1$ level as the major level. The $\pm nV_2$ level is defined as the high level of v_{cd}. In order to realize the control of the transferred power of the converter as well as the performance improvement, the four phase-shift control variables are defined as follows. D_{p1} is the duty cycle of the one-sided minor level of v_{ab}. D_{p2} is the duty cycle of the major level of v_{ab}. D_s is the duty cycle of the high level of v_{cd}. D_{ps} is the phase-shift ratio between the rising edge of the minor level of v_{ab} and that of the high level of v_{cd}. In addition, T_h is half a switching cycle.

Since forward power transfer and reverse power transfer are analyzed similarly, this article takes forward power transfer as an example. For forward power transfer, the fundamental phase-shift angle of the primary voltage and secondary voltage

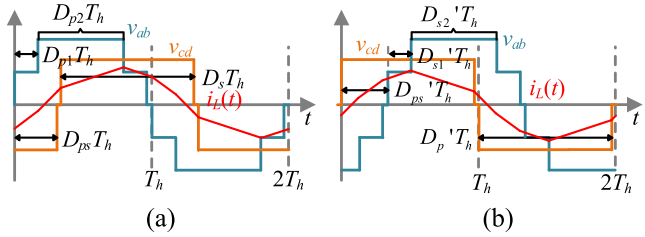

Fig. 3. Typical voltage and current waveforms. (a) Forward power transfer. (b) Reverse power transfer.

must be greater than 0. In order to reduce the reactive power of the converter, the fundamental phase-shift angle is limited to 90° [31]. Therefore, each control variable needs to satisfy the following constraints:

$$\begin{cases} D_{p1} \geq 0, D_{p2} \geq 0 \\ 2D_{p1} + D_{p2} \leq 1 \\ 0 \leq D_s \leq 1 \\ \frac{2D_{p1}+D_{p2}-D_s}{2} \leq D_{ps} \leq \frac{1+2D_{p1}+D_{p2}-D_s}{2}. \end{cases} \tag{3}$$

B. Bidirectional Power Transfer

Bidirectional energy flow capability is one of the significant advantages of DAB converters. When the 3/2LNPC-DAB converter operates in reverse power transfer, its voltage and current waveforms are exactly mirror images of those in forward power transfer, as shown in Fig. 3. When forward and reverse transfer the same power, their fundamental phase-shift angles are the negative of each other. Thus, the control variables during forward and reverse power transfer exhibit the relationship shown in the following equation:

$$\begin{cases} D_p' = D_s, D_{s1}' = D_{p1}, D_{s2}' = D_{p2} \\ D_{ps}' = D_{ps} + 2D_{p1} + D_{p2} - D_s. \end{cases} \tag{4}$$

C. ZVS Constraints

ZVS can significantly reduce the switching loss of the power switching device and thus improve the efficiency of the converter. Before the switching device is turned ON, ZVS can be realized if the inductor current can completely discharge

the junction capacitor of the switching device. However, DAB converters have regions where ZVS cannot be fully realized for all switching devices during the modal transition [32]. During the transition region, the inductor current cannot fully charge and discharge the junction capacitors of the switches within the dead time. Some bridge arms would work on quasi-zero-voltage switching (QZVS) or zero-current switching (ZCS) [14]. However, QZVS and ZCS still offer a significant reduction in switching losses compared to the hard switching. Furthermore, Song et al. [30] demonstrate that QZVS implementation in partial power switches yields higher converter efficiency compared to full ZVS operation. To achieve higher efficiency while maintaining the continuity of the analytical solution across power variations, this article adopts the QZVS conditions as the effective ZVS criteria.

Due to the symmetry of the inductor current at steady state, only the ZVS characteristics of the switching devices during half a switching cycle need to be considered. Therefore, the constraints for all switches to realize ZVS are shown as follows:

$$\begin{cases} i_{LN}(t_{p0}) \le 0, & i_{LN}(t_{p1}) \le 0, & i_{LN}(t_{p2}) \ge 0 \\ i_{LN}(t_{p3}) \ge 0, & i_{LN}(t_{s1}) \ge 0, & i_{LN}(t_{s2}) \le 0 \end{cases} \tag{5}$$

where $i_{LN}(t)$ represents the normalized inductor current. The normalized inductor current is defined as $i_{LN}(t) = i_L(t)/I_N$, where $I_N = nV_2T_h/(2L)$.

Notably, based on the switching sequence shown in Fig. 2, when $D_{p2} = 0$, switching devices P_5–P_8 will not operate. Thus, for $D_{p2} = 0$, the ZVS constraints of all switching devices are simplified as follows:

$$i_{LN}(t_{p0}) \le 0, \quad i_{LN}(t_{p3}) \ge 0, \quad i_{LN}(t_{s1}) \ge 0, \quad i_{LN}(t_{s2}) \le 0. \tag{6}$$

III. ZVS-Optimized Operating Modes

According to the different relative sizes of V_1 and nV_2, the voltage transfer ratio $k(= V_1/(nV_2))$ can be divided into three intervals: $0 < k < 1$, $1 < k < 2$, and $k > 2$. Based on the constraints of (3), the operating modes in each k-value interval of the 3/2LNPC-DAB converter can be classified into 13 modes. The only difference between the modes in different k-value intervals is the relative magnitude of the voltage. Taking $1 < k < 2$ as an example, all 13 operating modes are shown in Fig. 4.

Based on the ZVS constraints of (5), there are a total of five modes that can potentially achieve ZVS for all switching devices, as shown in Fig. 5. The modal constraints for each mode are shown in Table II. It is worth noting that not every mode can achieve ZVS for all switching devices in the full range of k. When $0 < k < 1$, only Modes IV and V may realize the ZVS of all switching devices. When $k > 2$, only Modes I and V may realize the ZVS of all switching devices. When $1 < k < 2$, the remaining four modes except Mode IV may realize ZVS for all switching devices.

The inductor current expressions and transferred power expressions for each mode need to be obtained via (1) and (2) in order to minimize the inductor peak current while realizing ZVS of all switching devices. After obtaining the inductor current at each switching action moment, the ZVS constraints for each mode are shown in Table III. The normalized transferred power is defined as $P_0 = P_{tr}/P_N$, where $P_N = nV_1V_2T_h/(4L)$. The nominal transferred power for each mode is shown in Table IV.

Combining the expressions of inductor current and transferred power as well as the ZVS constraints, the next section will analyze in detail the derivation process of the OQPS modulation for achieving full-range ZVS with minimum peak current.

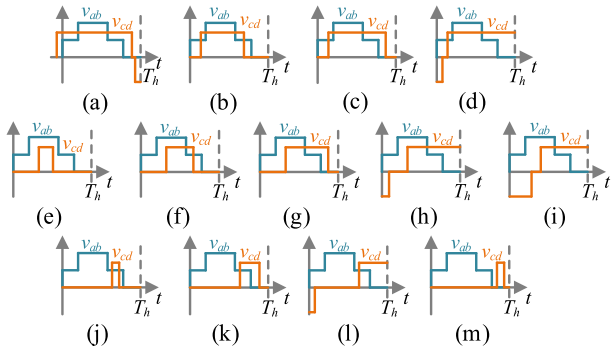

Fig. 4. (a)–(m) All operating modes for $1 < k < 2$.

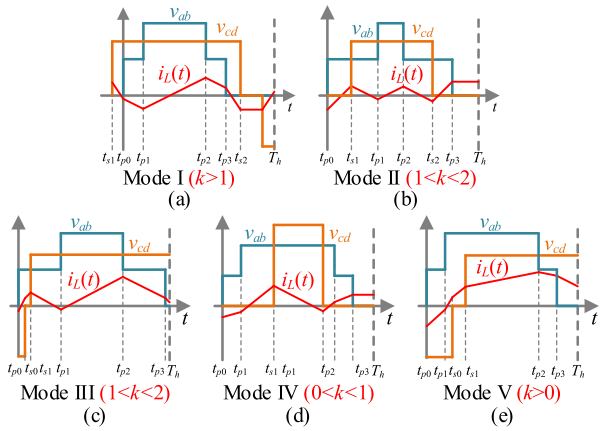

Fig. 5. Five modes that can potentially achieve ZVS for all switching devices. (a) Mode I. (b) Mode II. (c) Mode III. (d) Mode IV. (e) Mode V.

TABLE II
Modal Constraints for Modes I–V

Mode	Modal constraints
I	$D_{ps} \le 0$, $2D_{p1}+D_{p2} \le D_{ps}+D_s$
II	$0 \le D_{ps} \le D_{p1}$, $D_{p1}+D_{p2} \le D_{ps}+D_s \le 2D_{p1}+D_{p2}$
III	$1 \le D_{ps}+D_s$, $D_{ps} \le D_{p1}$
IV	$D_{p1} \le D_{ps}$, $D_{ps}+D_s \le D_{p1}+D_{p2}$
V	$1+D_{p1} \le D_{ps}+D_s$, $D_{ps} \le D_{p1}+D_{p2}$

IV. Derivation of the Proposed OQPS Modulation

A. Improved Lagrange Function and KKT Conditions

The optimization problem for the 3/2LNPC-DAB converter to minimize peak current while achieving ZVS for all switching

TABLE III
ZVS CONSTRAINTS FOR MODES I–V

Mode	ZVS constraints
I	$i_{LN\_I}(t_{p0}) = 2D_{ps} + D_s - k(D_{p1} + D_{p2}) \le 0,\ i_{LN\_I}(t_{p1}) = -2D_{p1} + 2D_{ps} + D_s - kD_{p2} \le 0,$ $i_{LN\_I}(t_{p2}) = -2D_{p1} + 2D_{ps} + D_s + (k-2)D_{p2} \ge 0,\ i_{LN\_I}(t_{p3}) = 2D_{ps} + D_s + (k-4)D_{p1} + (k-2)D_{p2} \ge 0,$ $i_{LN\_I}(t_{s1}) = D_s - k(D_{p1} + D_{p2}) \ge 0,\ i_{LN\_I}(t_{s2}) = -D_s + k(D_{p1} + D_{p2}) \le 0$
II	$i_{LN\_II}(t_{p0}) = D_s - k(D_{p1} + D_{p2}) \le 0,\ i_{LN\_II}(t_{p1}) = -2D_{p1} + 2D_{ps} + D_s - kD_{p2} \le 0,$ $i_{LN\_II}(t_{p2}) = -2D_{p1} + 2D_{ps} + D_s + (k-2)D_{p2} \ge I_z,\ i_{LN\_II}(t_{p3}) = -D_s + k(D_{p1} + D_{p2}) \ge 0,$ $i_{LN\_II}(t_{s1}) = D_s - k(D_{p1} + D_{p2} - D_{ps}) \ge 0,\ i_{LN\_II}(t_{s2}) = -D_s + k(-D_{p1} + D_{ps} + D_s) \le 0$
III	$i_{LN\_III}(t_{p0}) = 2 - 2D_{ps} - D_s - k(D_{p1} + D_{p2}) \le 0,\ i_{LN\_III}(t_{p1}) = -2D_{p1} + 2D_{ps} + D_s - kD_{p2} \le 0,$ $i_{LN\_III}(t_{p2}) = -2D_{p1} + 2D_{ps} + D_s + (k-2)D_{p2} \ge, 0,\ i_{LN\_III}(t_{p3}) = 2D_{ps} + D_s + (k-4)D_{p1} + (k-2)D_{p2} \ge 0,$ $i_{LN\_III}(t_{s1}) = D_s - k(D_{p1} + D_{p2} - D_{ps}) \ge 0,\ i_{LN\_III}(t_{s2}) = -D_s + k(1 + D_{p1} + D_{p2} - D_{ps} - D_s) \le 0$
IV	$i_{LN\_IV}(t_{p0}) = D_s - k(D_{p1} + D_{p2}) \le 0,\ i_{LN\_IV}(t_{p1}) = D_s - kD_{p2} \le 0,$ $i_{LN\_IV}(t_{p2}) = -D_s + kD_{p2} \ge 0,\ i_{LN\_IV}(t_{p3}) = -D_s + k(D_{p1} + D_{p2}) \ge 0,$ $i_{LN\_IV}(t_{s1}) = D_s - k(2D_{p1} + D_{p2} - 2D_{ps}) \ge 0,\ i_{LN\_IV}(t_{s2}) = -D_s + k(-2D_{p1} - D_{p2} + 2D_{ps} + 2D_s) \le 0$
V	$i_{LN\_V}(t_{p0}) = 2 - 2D_{ps} - D_s - k(D_{p1} + D_{p2}) \le 0,\ i_{LN\_V}(t_{p1}) = 2 + 2D_{p1} - 2D_{ps} - D_s - kD_{p2} \le 0,$ $i_{LN\_V}(t_{p2}) = -2D_{p1} + 2D_{ps} + D_s + (k-2)D_{p2} \ge 0,\ i_{LN\_V}(t_{p3}) = 2D_{ps} + D_s + (k-4)D_{p1} + (k-2)D_{p2} \ge 0,$ $i_{LN\_V}(t_{s1}) = D_s - k(2D_{p1} + D_{p2} - 2D_{ps}) \ge 0,\ i_{LN\_V}(t_{s2}) = -D_s + k(2 + 2D_{p1} + D_{p2} - 2D_{ps} - 2D_s) \le 0$

TABLE IV
NOMINAL TRANSFERRED POWER FOR MODES I–V

Mode	Nominal transferred power P_0
I	$-4D_{p1}^2 - 2D_{p2}^2 - 6D_{p1}D_{p2} + 4D_{p1}D_{ps} + 2D_{p1}D_s + 4D_{p2}D_{ps} + 2D_{p2}D_s$
II	$-D_{p2}^2 + D_s^2 - 2D_{p1}D_{p2} - 2D_{p1}D_s + 2D_{p2}D_{ps} + 2D_{ps}D_s$
III	$-4D_{p1}^2 - 2D_{p2}^2 - 2D_{ps}^2 - D_s^2 - 6D_{p1}D_{p2} + 4D_{p1}D_{ps} + 2D_{p1}D_s + 4D_{p2}D_{ps} + 2D_{p2}D_s - 2D_{ps}D_s + 2D_{ps} + 2D_s - 1$
IV	$2D_s^2 - 4D_{p1}D_s - 2D_{p2}D_s + 4D_{ps}D_s$
V	$-6D_{p1}^2 - 2D_{p2}^2 - 4D_{ps}^2 - 2D_s^2 - 6D_{p1}D_{p2} + 8D_{p1}D_{ps} + 4D_{p1}D_s + 4D_{p2}D_{ps} + 2D_{p2}D_s - 4D_{ps}D_s - 2D_{p1} + 4D_{ps} + 4D_s - 2$

devices can be described as follows:

$$\begin{aligned} \min \quad & I_0(\boldsymbol{D}) \\ \text{s.t.} \quad & P_0(\boldsymbol{D}) - P_0^* = 0 \\ & g_i(\boldsymbol{D}) \le 0, \quad i = 1, 2, \ldots, r \end{aligned} \tag{7}$$

where $\boldsymbol{D} = (D_{p1}, D_{p2}, D_{ps}, D_s)$ represents a set of control variables. $I_0(\boldsymbol{D})$ and $P_0(\boldsymbol{D})$, respectively, represent the nominal peak current and the nominal transferred power expressed by a set of control variables $\boldsymbol{D}$. $P_0{}^*$ represents the ideal nominal transfer power. $g_i(\boldsymbol{D})$ represents the inequality constraints of control variables. r is the number of inequality constraints. The inequality constraints contain control variable definition constraints, modal constraints, and ZVS constraints, as shown in (5), Table II, and Table IV, respectively. The optional region of $\boldsymbol{D}$ that satisfies all inequality constraints is the feasible region of $\boldsymbol{D}$.

The Lagrange function and KKT conditions provide an efficient solution for solving optimization problems with constraints. The traditional Lagrange function and the KKT conditions can be described as follows:

$$L(\boldsymbol{D}, \lambda, \mu_i) = I_0(\boldsymbol{D}) + \lambda(P_0(\boldsymbol{D}) - P_0^*) + \sum_{i=0}^{r} \mu_i g_i(\boldsymbol{D}) \tag{8}$$

$$\begin{cases} \dfrac{\partial L}{\partial \boldsymbol{D}}\Big|_{\boldsymbol{D}=\boldsymbol{D}^*} = 0, P_0(\boldsymbol{D}^*) - P_0{}^* = 0, \mu_i g_i(\boldsymbol{D}^*) = 0 \\ g_i(\boldsymbol{D}^*) \le 0, \lambda \ne 0, \mu_i \ge 0 \end{cases} \tag{9}$$

where λ and u_i represent the Lagrange multipliers. $\boldsymbol{D}^*$ represents a set of optimal control variables that is expected to satisfy the KKT conditions in (9).

In the process of solving the KKT conditions for the symbolic variables, it is normally divided into two steps. First, all the solution sets are found through the equation constraints, and then, the optimal solutions are filtered based on the inequality constraints. Theoretically, directly solving the equation constraints of the traditional KKT conditions yields $\sum_{i=0}^{q-1} C_r^i$ sets of analytical solutions, where q is the number of control variables.

It is extremely challenging to solve the traditional KKT conditions directly for each mode due to the large number of inequality constraints and control variables. Taking Mode I as an example, the number of inequality constraints reaches as many as 15. Solving the equation constraint of the traditional KKT conditions will yield 576 sets of solutions. Therefore, it is impractical to solve the traditional KKT conditions directly.

In order to lower the difficulty of solving the KKT conditions, an improved Lagrange function and KKT conditions are

TABLE V
COMPARISON OF TRADITIONAL LAGRANGE FUNCTION WITH KKT CONDITIONS AND IMPROVED LAGRANGE FUNCTION WITH KKT CONDITIONS

	Traditional	Improved
Lagrange function expansion term	$2+r$	$2+m$
Inequality constraints of KKT conditions	$2r$	r
Solution set of the equation constraint of the KKT conditions	$\sum_{i=0}^{q-1} C_r^i$	1

proposed, which can be described as follows:

$$L(\boldsymbol{D},\lambda,\mu_i,u_j)=I_0(\boldsymbol{D})+\lambda(P_0(\boldsymbol{D})-P_0^*)+\sum_{i=0}^{m}\mu_i g_i(\boldsymbol{D})+\sum_{j=0}^{n}\mu_j g_j(\boldsymbol{D})=I_0(\boldsymbol{D})+\lambda(P_0(\boldsymbol{D})-P_0^*)+\sum_{i=0}^{m}\mu_i g_i(\boldsymbol{D}) \tag{10}$$

$$\begin{cases}\frac{\partial L}{\partial \boldsymbol{D}}\big|_{\boldsymbol{D}=\boldsymbol{D}^*}=0, P_0(\boldsymbol{D}^*)-P_0{}^*=0, \quad \lambda\neq 0\\ g_i(\boldsymbol{D}^*)=0, \quad \mu_i\geq 0, \quad g_j(\boldsymbol{D}^*)\leq 0, \quad \mu_j=0.\end{cases} \tag{11}$$

$\sum_{i=0}^{r}\mu_i g_i(\boldsymbol{D})$ in (8) can be decomposed into $\sum_{i=0}^{m}\mu_i g_i(\boldsymbol{D})+\sum_{j=0}^{n}\mu_j g_j(\boldsymbol{D})$ in (10), where $r=m+n$. $g_i(\boldsymbol{D}^*)=0$ in (10) is the boundary of the feasible region to be satisfied by the optimal solution obtained by numerical optimization. If the optimal solution appears on the boundary of the feasible region, $g_i(\boldsymbol{D})=0$ and $u_i\geq 0$. Conversely, if the optimal solution appears inside the boundary of the feasible region, $g_j(\boldsymbol{D})\leq 0$ and $u_j=0$. In this way, the number of inequality constraints for the KKT conditions can be reduced from $2r$ to r. Solving the equality constraint of the improved KKT conditions will only yield one set of valid analytical solutions. In this case, the range of transferred power corresponding to this set of optimal solutions can be derived directly by inequality constraints. Comparison of the traditional Lagrange function with the KKT conditions and the improved Lagrange function with the KKT conditions is shown in Table V.

B. Numerical Optimization Analysis for $1 < k < 2$

There are different operating modes in different k-value intervals. Therefore, the analytical expressions of the OQPS modulation for different k-value intervals are different. Since the analytical steps for different k-value intervals are consistent, this article takes the interval $1 < k < 2$ as an example. The analytical expressions of all control variables of the OQPS modulation in all k-value ranges are then given for reference and application.

When $1 < k < 2$, there is a total of four modes that may achieve ZVS for all switching devices. However, these four modes are not necessarily all optimal modes. In order to screen out the optimal modes, the minimum peak current of each mode for achieving the ZVS of all switching devices can be obtained by numerical optimization. The minimum nominal peak current

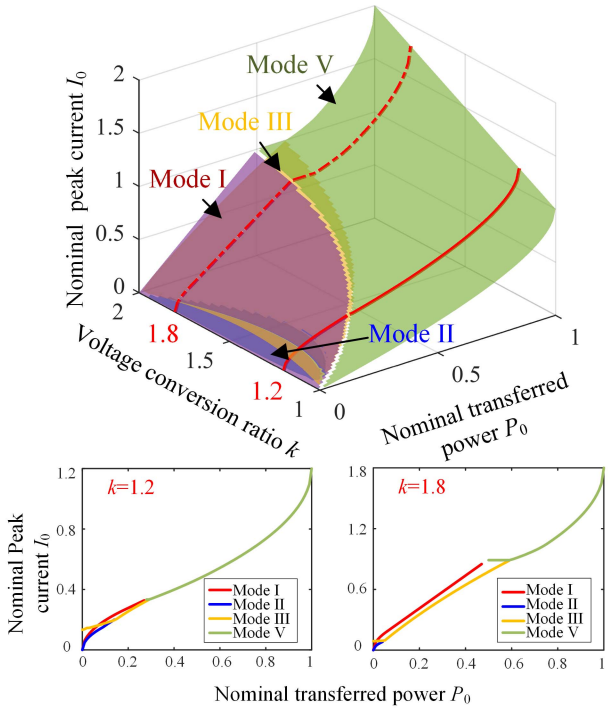

Fig. 6. Minimum nominal peak current for each mode in achieving ZVS.

TABLE VI
BOUNDARIES OF THE FEASIBLE REGION FOR ACHIEVING THE OPTIMAL SOLUTION FOR EACH MODE

Mode	Stage	Boundaries of the feasible region
II	Stage 1	$i_{LN\_II}(t_{p1})=0, i_{LN\_II}(t_{p2})=i_{LN\_II}(t_{s1})$
	Stage 2	$i_{LN\_II}(t_{p0})=i_{LN\_II}(t_{p1})=0, 2D_{p1}+D_{p2}=1$
III	Stage 3	$i_{LN\_III}(t_{p0})=i_{LN\_III}(t_{p1})=0, 2D_{p1}+D_{p2}=1$
	Stage 4	$i_{LN\_III}(t_{p1})=0, 2D_{p1}+D_{p2}=1, D_s=1$
V	Stage 5	$i_{LN\_V}(t_{p1})=0, 2D_{p1}+D_{p2}=1, D_s=1$
	Stage 6	$2D_{p1}+D_{p2}=1, D_s=1$

surfaces for each mode in achieving ZVS are given in Fig. 6. Exceptionally, the minimum nominal peak current when achieving ZVS for each mode at $k=1.2$ and $k=1.8$ is plotted separately for better observation of the results. It can be found that for the same transferred power, it is always possible to find operating points in Modes II and III with less peak current than those in Mode I. Therefore, Mode I is not the optimal operating mode for $1 < k < 2$. Conversely, Modes II, III, and V together form the optimal operating modes for $1 < k < 2$.

Based on the results of numerical optimization, all inequality constraints can be verified to check whether they are converted into equality constraints, so as to determine whether the optimal solution appears on the boundary of the feasible region. It is verified that there are six power stages for $1 < k < 2$ in total, based on the differences in the operating modes and the feasible region boundaries satisfied by the optimal solution. The feasible region boundaries satisfied by the optimal solution for each mode are shown in Table VI.

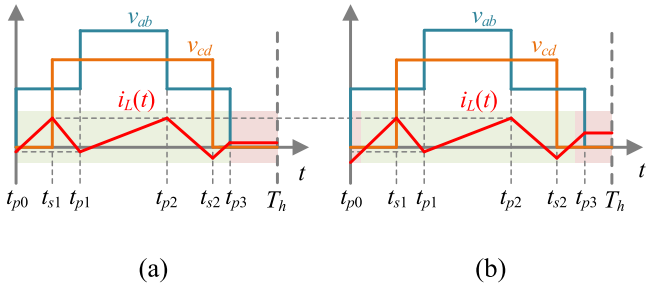

Fig. 7. Two cases of achieving ZVS as well as peak current minimization in Stage 1. (a) $i_{LN\_II}(t_{p0}) = 0$. (b) $i_{LN\_II}(t_{p0}) < 0$.

C. Analytic Solution for Optimal Modulation

According to the boundaries of the feasible region for achieving the optimal solution in Table VI, the analytical solution of optimal modulation can be solved based on the improved Lagrange function and the KKT conditions in Section IV-A. The analytic solutions of the optimal modulation are all unique, except for Stage 1. The reason and solution for the nonunique analytical solution of the optimal modulation in Stage 1 are elaborated as follows.

For Stage 1, the improved Lagrange function and KKT conditions are shown in (12) shown at the bottom of this page and (13) shown at the bottom of this page, respectively. Solving the KKT conditions in (13) yields analytical expressions for each control variable, as shown in (14) shown at the bottom of this page. From (14), it can be found that D_{ps} will vary synchronously with D_{p1}. This means that the optimal solution to achieve the minimum peak current while achieving ZVS for all switching devices is not unique, as shown in Fig. 7. Regardless of the variation of D_{ps} and D_{p1}, there is always a section of the same inductor current waveform, as shown in the green area in Fig. 7. Obviously, if $i_{LN}(t_{p0}) = 0$, the rms value of the inductor current in the red region will be minimized. In order to obtain a unique set of deterministic analytical solutions, the boundary constraint of the feasible region $i_{LN}(t_{p0}) = 0$ is added to the current solution to further reduce the conduction losses. Therefore, the feasible region boundaries satisfied by the optimal solution for Stage 1 in Table V are corrected as follows:

$$i_{LN\_II}(t_{p0}) = i_{LN\_II}(t_{p1}) = 0, \quad i_{LN\_II}(t_{p2}) = i_{LN\_II}(t_{s1}). \tag{15}$$

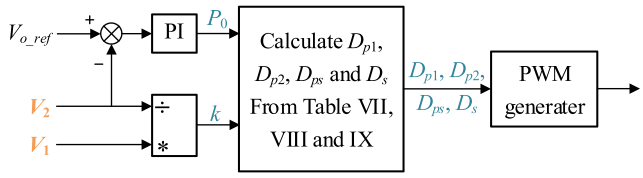

Fig. 8. Closed-loop control for OQPS modulation.

The analytical solution for optimal modulation of Stage 1 can be obtained by reconstructing the improved Lagrange function and solving the improved KKT conditions. The power range of Stage 1 can be derived by solving the inequality constraints of the improved KKT conditions. The optimal solution for the remaining power stages can be solved by the same method. The analytical expressions of the optimal modulation for $1 < k < 2$ is shown in Table VII. According to the similar analytical method, the analytical expressions of optimal modulation for $k < 1$ and $k > 2$ can be derived, as shown in Tables VIII and IX, respectively.

D. Closed-Loop Control

To achieve a constant output voltage, the closed-loop control structure for OQPS modulation is designed, as shown in Fig. 8. Only the input voltage and output voltage need to be sampled to achieve closed-loop control of the converter. The voltage transfer ratio k is determined by two voltage sampling values. The output signal of the proportional–integral (PI) controller is regarded as a virtual nominal transferred power P_0. In practical applications, both P_0 and k must be limited to prevent overflow during computation. Based on the analytical solution for OQPS modulation in Tables VII, VIII, and IX, each control variable can be computed in the microcontroller. Finally, gate signals are generated from four control variables.

V. Analysis of Power Losses

The power losses of the 3/2LDNPC-DAB converter comprise conduction and switching losses of active switching devices, power diode losses, magnetic component losses, and resistor–capacitor losses.

A. Conduction Losses of Active Switching Devices

Conduction losses are divided into conduction losses of primary active switching devices P_{on_p} and secondary active

$$L(\boldsymbol{D}, \lambda, \mu_i, u_j) = i_{LN\_II}(t_{p2}) + \lambda(P_0(\boldsymbol{D}) - P_0^*) + u_1 i_{LN\_II}(t_{p1}) + u_2(i_{LN\_II}(t_{s1}) - i_{LN\_II}(t_{p2})) \tag{12}$$

$$\left.\frac{\partial L}{\partial \boldsymbol{D}}\right|_{\boldsymbol{D}=\boldsymbol{D}^*} = 0, P_0(\boldsymbol{D}^*) - P_0{}^* = 0, \quad \lambda \neq 0, \quad i_{LN\_II}(t_{p2}) = 0, \quad i_{LN\_II}(t_{s1}) = i_{LN\_II}(t_{p2}), \quad \mu_i \geq 0, \quad g_j(\boldsymbol{D}^*) \leq 0 \tag{13}$$

$$\begin{cases} D_{p2} = \frac{I_0\left(k^2-4k+2\right)}{(k-1)(k^2-5k+2)} - \frac{1}{(k-1)(k^2-5k+2)}\sqrt{I_0{}^2k^2 + (k-1)(k-2)(k^2-5k+2)P_0} \\ D_{ps} = D_{p1} + \frac{2I_0\left(k^2-4k+2\right)}{(k-2)(k^2-5k+2)} - \frac{2}{(k-2)(k^2-5k+2)}\sqrt{I_0{}^2k^2 + (k-1)(k-2)(k^2-5k+2)P_0} \\ D_{s1} = \frac{I_0(4-k(4-k)(3-2k))}{(k-1)(k-2)(k^2-5k+2)} - \frac{\left(k^2-6k+4\right)}{(k-1)(k-2)(k^2-5k+2)}\sqrt{I_0{}^2k^2 + (k-1)(k-2)(k^2-5k+2)P_0} \end{cases} \tag{14}$$

TABLE VII
ANALYTICAL EXPRESSIONS OF PROPOSED OQPS MODULATION FOR $1 < K < 2$ IN THE FULL POWER RANGE

Power range	D_{p1}	D_{p2}	D_{ps}	D_s
$0 \le P_0 < P_{A1}$	$\frac{4(k-1)}{k(2-k)}A_1$	A_1	$\frac{2(k-1)}{k}A_1$	$\frac{k^2-6k+4}{k-2}A_1$
$P_{A1} \le P_0 \le P_{A2}$	$\frac{4+3k}{4(2+k)}-\frac{1}{4(2+k)}A_2$	$\frac{-k}{2(2+k)}+\frac{1}{2(2+k)}A_2$	$\frac{(2-k)(4+3k)}{8(2+k)}-\frac{2-k}{8(2+k)}A_2$	$\frac{k(4+k)}{4(2+k)}+\frac{k}{4(2+k)}A_2$
$P_{A2} \le P_0 < P_{A3}$	$\frac{2(k-1)}{3k-2}$	$\frac{2-k}{3k-2}$	$\frac{(k-1)(2-k)}{2(3k-2)}+\frac{1}{2(3k-2)}A_3$	$1-\frac{1}{3k-2}A_3$
$P_{A3} \le P_0 < P_{A4}$	$\frac{4-k}{2(3-k)}-\frac{1}{2(3-k)}A_4$	$\frac{-1}{3-k}+\frac{1}{3-k}A_4$	$\frac{1-k}{2(3-k)}+\frac{k-1}{2(3-k)}A_4$	1
$P_{A4} \le P_0 < P_{A5}$	$\frac{k(1+k)}{A_5}-\frac{1}{2A_5}A_6$	$\frac{3+2k}{A_5}+\frac{1}{A_5}A_6$	$\frac{3+3k+2k^2}{2A_5}-\frac{1+k}{2A_5}A_6$	1
$P_{A5} \le P_0 \le 1$	$(k-1)\sqrt{\frac{1-P_0}{3-4k+2k^2}}$	$1-2(k-1)\sqrt{\frac{1-P_0}{3-4k+2k^2}}$	$\frac{1}{2}-\frac{1}{2}\sqrt{\frac{1-P_0}{3-4k+2k^2}}$	1

$$A_1=\sqrt{\frac{(k-2)P_0}{(k-1)(k^2-5k+2)}},A_2=\sqrt{k^2+\frac{8(2+k)}{(k-1)}P_0},A_3=\sqrt{(k-1)(2-k)(2+k+k^2)-2(2-3k)^2P_0},$$

$$A_4=\sqrt{1+\frac{2(3-k)}{k-1}P_0},A_5=3+4k+2k^2,A_6=\sqrt{2(k+1)(k+3)-2A_5P_0},$$

$$P_{A1}=\frac{k^2(k-1)(k-2)(k^2-5k+2)}{(8-10k+k^2)^2},P_{A2}=\frac{(k-1)(2-k)(2-k+k^2)}{(3k-2)^2},P_{A3}=\frac{(k-1)(2-k)(2+k+k^2)}{2(3k-2)^2},P_{A4}=\frac{(k-1)(3+k)}{2k^2},P_{A5}=\frac{(k-1)(-1-k+6k^2+2k^3)}{(2k^2-1)^2}$$

TABLE VIII
ANALYTICAL EXPRESSIONS OF THE PROPOSED OQPS MODULATION FOR $0 < K < 1$ IN THE FULL POWER RANGE

Power range	D_{p1}	D_{p2}	D_{ps}	D_s
$0 \le P_0 \le 2k(1-k)$	0	$\frac{1}{2k(1-k)}\sqrt{2k(1-k)P_0}$	$\frac{1}{2k}\sqrt{2k(1-k)P_0}$	$\frac{1}{2(1-k)}\sqrt{2k(1-k)P_0}$
$2k(1-k) \le P_0 \le 1$	0	1	$\frac{1}{2}-\frac{2k-1}{2}\sqrt{\frac{1-P_0}{1-2k+2k^2}}$	$1-(1-k)\sqrt{\frac{1-P_0}{1-2k+2k^2}}$

TABLE IX
ANALYTICAL EXPRESSIONS OF THE PROPOSED OQPS MODULATION FOR $K > 2$ IN THE FULL POWER RANGE

Power range	D_{p1}	D_{p2}	D_{ps}	D_s
$0 \le P_0 < P_{B1}$	$\sqrt{\frac{P_0}{2(k-2)}}$	0	0	$k\sqrt{\frac{P_0}{2(k-2)}}$
$P_{B1} \le P_0 \le P_{B2}$	$\frac{1}{2}-\frac{k-2}{2}\sqrt{\frac{1-2P_0}{8-4k+k^2}}$	0	$\frac{1}{2}-\frac{k}{2}\sqrt{\frac{1-2P_0}{8-4k+k^2}}$	1
$P_{B2} \le P_0 < P_{B3}$	$\frac{k-1}{2k}-\frac{1}{2k}\sqrt{k^2+2k-3-2k^2P_0}$	$\frac{1}{k}$	$\frac{k-1}{2k}-\frac{1}{2k}\sqrt{k^2+2k-3-2k^2P_0}$	1
$P_{B3} \le P_0 < P_{B4}$	$\frac{k(1+k)}{3+4k+2k^2}-\frac{-2-2k+k^3}{3+4k+2k^2}B_1$	$\frac{3+2k}{3+4k+2k^2}+\frac{2+k}{3+4k+2k^2}B_1$	$\frac{3+3k+2k^2}{2(3+4k+2k^2)}+\frac{4+2k-k^2-2k^3}{2(3+4k+2k^2)}B_1$	1
$P_{B4} \le P_0 \le 1$	$\sqrt{\frac{1-P_0}{3-2k+k^2}}$	$1-k\sqrt{\frac{1-P_0}{3-4k+2k^2}}$	$\frac{1}{2}-\frac{k-1}{2}\sqrt{\frac{1-P_0}{3-4k+2k^2}}$	1

$$B_1=\sqrt{\frac{3+4k+k^2-(3+4k+2k^2)P_0}{8+4k-2k^2-2k^3+k^4}},P_{B1}=\frac{2(k-2)}{k^2},P_{B4}=\frac{1+2k+4k^3}{(1+k+k^2)^2}.$$

When $2 < k \le 4.36$, $P_{B2}=\frac{4+4k-k^2}{16}+\frac{(k-2)^2\sqrt{(8-4k+k^2)(-8+4k+k^2)}}{16k^2},P_{B3}=\frac{2(3+k)(-4+2k+k^2)}{k^2(2+k)^2}$;

when $k > 4.36$, $P_{B2}=P_{B3}=\frac{-2(16+16k-38k^2-51k^3-18k^4+k^5+2k^6)}{(8+12k+7k^2)^2}+\frac{2k(1+2k)\sqrt{(8-4k+k^2)(4+6k+k^2)(8+4k-2k^2-2k^3+k^4)}}{(8+12k+7k^2)^2}$.

switching devices $P_{\text{on\_}s}$. The ON-resistances of the primary and secondary active switching devices are denoted as R_{dson_p} and R_{dson_s}, respectively.

For the primary active switching devices, their on-time depends on the adopted optimized modulation due to the presence of NPC full-bridge power diodes. Thus, their rms currents need to be evaluated independently, and the conduction losses of these primary devices are calculated as follows:

$$P_{\text{on\_}p} = \sum_{i=1}^{8} {I_{\text{rms\_}Pi}}^2 R_{dson\_p} \tag{16}$$

where $I_{\text{rms\_}Pi}$ is the rms current of primary switching device P_i. Each secondary active switching device has a 50% duty cycle. Thus, the conduction losses of these secondary devices are expressed as follows:

$$P_{\text{on\_}s} = 2{I_{\text{rms\_}s}}^2 R_{dson\_s} \tag{17}$$

where $I_{\text{rms\_}s}$ is the rms current on the secondary side of the transformer.

B. Switching Losses of Active Switching Devices

The switching losses of active switching devices include turn-ON losses $P_{\text{turn-on}}$ and turn-OFF losses $P_{\text{turn-off}}$. Under the proposed OQPS modulation, all switching devices operate in ZVS or QZVS. Turn-ON losses of the devices are zero under ZVS. To achieve complete ZVS, the switching current I_{sw} must satisfy

$$|I_{\text{sw}}| \geq \frac{V_{\text{dc}} C_{oss}(V_{\text{dc}})}{t_d} \tag{18}$$

where V_{dc} denotes the dc bus voltage borne by the half-bridge containing the switching device. $C_{oss}(V_x)$ is the junction capacitance of the switching device at V_x. t_d is the dead time.

Otherwise, the switching devices operate under QZVS. The turn-ON losses under QZVS can be expressed as follows [33]:

$$\begin{aligned} P_{\text{turn-on}} &= f_s \\ &\times \begin{pmatrix} E_{oss}(\frac{V_{\text{dc}} t_d}{I_{\text{sw}}}) + E_{oss}(V_{\text{dc}} - \frac{V_{\text{dc}} t_d}{I_{\text{sw}}}) - E_{oss}(V_{\text{dc}}) \\ +V_{\text{dc}}(Q_{oss}(V_{\text{dc}}) - Q_{oss}(\frac{V_{\text{dc}} t_d}{I_{\text{sw}}})) \end{pmatrix} \end{aligned} \tag{19}$$

where $E_{oss}(V_x)$ represents the energy stored in the junction capacitor of the switching device at the voltage V_x. f_s is the switching frequency.

Regardless of the operating state of the switching device, the turn-OFF losses can be calculated using the following equation [34]:

$$P_{\text{turn-off}} = \frac{1}{2} V_{\text{dc}} I_{\text{sw}} t_{\text{off}} f_s \tag{20}$$

where t_{off} is the turn-OFF time of the switching device.

C. Power Diode Losses

Power diode losses can be divided into conduction losses and reverse recovery losses. For SiC Schottky diodes, reverse recovery losses can be neglected. Thus, only the conduction losses need to be considered. When conducting, a diode is equivalent to a series connection of a voltage source and a resistor, with its equivalent voltage drop given as follows:

$$V_{\text{diode}} = V_f + R_f i_d \tag{21}$$

where the voltage of the equivalent voltage source V_f and the resistor R_f can be obtained from the diode's datasheet. i_d represents the instantaneous current flowing through the diode. Thus, the power diode losses P_{diode} can be expressed as follows:

$$P_{\text{diode}} = \sum_{j=1}^{4} (V_f I_{\text{mean\_}Dj} + {I_{\text{rms\_}Dj}}^2 R_{\text{on\_}d}) \tag{22}$$

where $I_{\text{mean\_}Dj}$ and $I_{\text{rms\_}Dj}$ represent the mean current and rms current of the power diode D_j, respectively.

D. Magnetic Component Losses

In the design of the DAB converter, the leakage inductor of the transformer can be designed as the power transfer inductor. Thus, an external series inductor is not required. The magnetic component of the converter consists solely of the transformer. The magnetic component losses include core losses and copper losses. According to [35], the core losses can be calculated using the improved generalized Steinmetz equation, as follows:

$$\begin{cases} P_{\text{core}} = \frac{V_e}{2T_h} \int_0^{2T_h} k_i \left|\frac{dB}{dt}\right|^{\alpha} (\Delta B)^{\beta-\alpha} dt \\ k_i = \frac{k_s}{(2\pi)^{\alpha-1} \int_0^{2\pi} |\cos\theta|^{\alpha} 2^{\beta-\alpha} d\theta} \end{cases} \tag{23}$$

where V_e is the volume of the core. *dB/dt* is the rate of change of magnetic flux density. ΔB is the peak-to-peak value of magnetic flux density. k_s, α, and β are the Steinmetz coefficients of the core material.

In the high-frequency transformer, the skin effect and proximity effect of the windings cannot be neglected. The ac resistance of the Litz wire windings can be calculated using Tourkhani's formula [36]. The copper losses of the transformer are expressed as follows:

$$P_{\text{copper}} = {I_{\text{rms\_}s}}^2 (n^2 R_{tr\_p\_\text{ac}} + R_{tr\_s\_\text{ac}}) \tag{24}$$

where $R_{tr\_p\_\text{ac}}$ and $R_{tr\_s\_\text{ac}}$ are the ac resistances of the primary and secondary windings of the transformer, respectively.

E. Resistor–Capacitor Losses

To achieve capacitor voltage balancing of the NPC full bridge, balancing resistors are connected in parallel across the dc-link capacitors. The losses of these resistors are nonnegligible and can be expressed as follows:

$$P_R = \frac{{V_1}^2}{2R_{\text{balance}}} \tag{25}$$

where R_{balance} is the resistance value of the balancing resistor connected in parallel across the dc-link capacitors.

The input and output capacitors of the DAB converter carry current ripple at the switching frequency. The losses incurred in these capacitors can be expressed as follows:

$$P_C = {I_{\text{rms\_}pc}}^2 R_{pc} + {I_{\text{rms\_}sc}}^2 R_{sc} \tag{26}$$

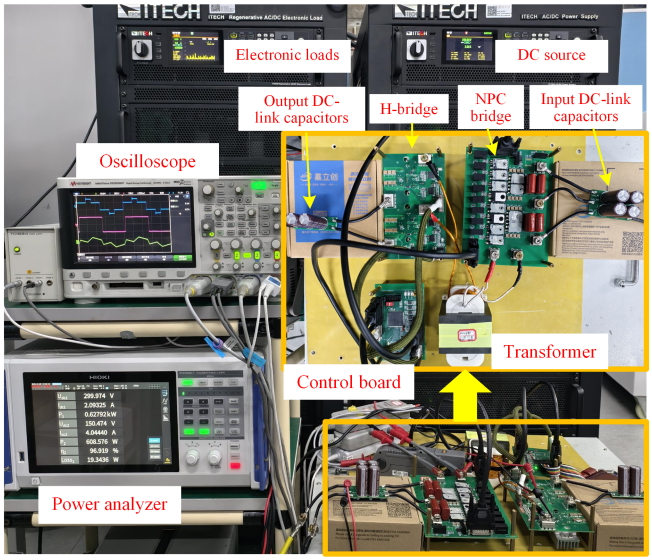

Fig. 9. Prototype platform of a 3/2LNPC-DAB converter.

TABLE X
MAIN PARAMETERS OF THE PROTOTYPE

Parameters	Values
Rated power P	1.6 kW
Input voltage V_1	120–400 V
Output voltage V_2	80–300 V
Transformer ratio n	26:21
Transformer leakage inductance L	40 μH
Switching frequency f_{sw}	50 kHz
DC-link capacitors C_{p1}, C_{p2}, and C_s	440 μF

where $I_{\mathrm{rms\_}pc}$ and $I_{\mathrm{rms\_}sc}$ are the rms current flowing through the input capacitors and output capacitors, respectively. R_{pc} and R_{sc} are the equivalent series resistances of the input and output capacitors, respectively.

VI. EXPERIMENTAL VALIDATION

A 1.6-kW prototype platform, shown in Fig. 9, was constructed to verify the effectiveness of the proposed OQPS modulation. The main parameters of the prototype are shown in Table X. OQPS modulation is implemented on the controller TMS320F28377. In the prototype, SiC power switches C3M0025065K and SiC power diodes C3D16065D jointly form the primary NPC full bridge. For the secondary full bridge, two SiC power half-bridge modules CAB011M12FM3 are employed. The transformer leakage inductor is used as the DAB inductor, and there is no external series inductor. The leakage inductance value is 40 μH, and the transformer core material is N97.

A. Soft-Switching Implementation of OQPS Modulation

Fig. 10 shows the experimental waveforms at different transferred powers during forward power transfer under $V_1 = 300$ V and $V_2 = 150$ V, i.e., $k = 1.62$. When $P_0 = 0.06$, the converter operates in Stage 1, as shown in Fig. 10(a). The switching devices P_1, P_4, P_5, and P_8 are operating at ZCS. The rest of the switching devices are operating at ZVS. For Stages 2 and 3, the power range is narrow, and the soft-switching implementation is the same as in Stage 1. When $P_0 = 0.17$, the converter operates in Stage 4, as shown in Fig. 10(b). In this case, the switching devices P_5 and P_8 operate at ZCS, and the rest of the switching devices operate at ZVS. When $P_0 = 0.56$, the converter operates in Stage 5, as shown in Fig. 10(c). The soft-switching implementation of the switching devices is consistent with Stage 4. The difference is that $D_{ps} < D_{p1}$ in Stage 4, while $D_{ps} > D_{p1}$ in Stage 5. When $P_0 = 0.71$, the converter operates in Stage 6, as shown in Fig. 10(d), where all the switching devices achieve ZVS.

Fig. 11 shows the experimental waveforms at different transferred powers during forward power transfer under $V_1 = 300$ V and $V_2 = 100$ V, i.e., $k = 2.42$. When $P_0 = 0.08$, the converter operates in Stage 1, as shown in Fig. 11(a). Switching devices P_1, P_4, and S_1–S_4 are operating at ZCS. Switching devices P_2 and P_3 are operating at ZVS. Switching devices P_5∼P_8 are inactive and have no switching loss. When $P_0 = 0.26$, the converter operates in Stage 2, as shown in Fig. 11(b). Except that switching devices P_5–P_8 are in an inactive state with no switching losses, the remaining switching devices all achieve ZVS. When $P_0 = 0.51$, the converter operates in Stage 3, as shown in Fig. 11(c). In this case, the switching devices P_5, P_8, and S_1–S_4 operate at ZCS, and the rest of the switching devices operate at ZVS. For Stage 4, only switching devices P_5 and P_8 operate at ZCS, while the rest achieve ZVS. Since the experimental waveform of Stage 4 is highly similar to that of Stage 3, it is not presented in Fig. 11. When $P_0 = 0.82$, the converter operates in Stage 5, as shown in Fig. 10(d), where all the switching devices achieve ZVS.

The proposed OQPS modulation is also applicable to reverse power transfer, where the four control variables can be derived from (4). The experimental results of reverse power transfer are presented in Figs. 12 and 13. Fig. 12 shares the same operating voltages as Fig. 10. At the same transferred power, the voltage and current waveforms of forward and reverse power transfer are fully symmetric, and the realization of ZVS is also symmetric. Fig. 13 also shares the same operating voltages as Fig. 11, with symmetric waveforms.

B. Comparison of Various Modulation Strategies

In order to verify the effectiveness of the proposed OQPS modulation to enhance the efficiency and reduce the peak current, various phase-shift modulations, including TPS-MCS modulation in [27], QPS-MCS modulation in [29], and QPS-ZVS modulation in [30], are compared. The comparison of the theoretical peak current for the four modulation strategies at $k = 0.7, 1.5, 3$ is shown in Fig. 14. When $k = 0.7$, all modulations achieve the same peak current at the same transferred power, as their analytical expressions for optimized modulations are consistent when $k < 1$. When $k > 1$, the proposed OQPS modulation attains the minimum peak current over most transferred power ranges. Near medium power, the QPS-MCS modulation may achieve a smaller peak current than the OQPS modulation, as it only takes peak current as the optimization objective

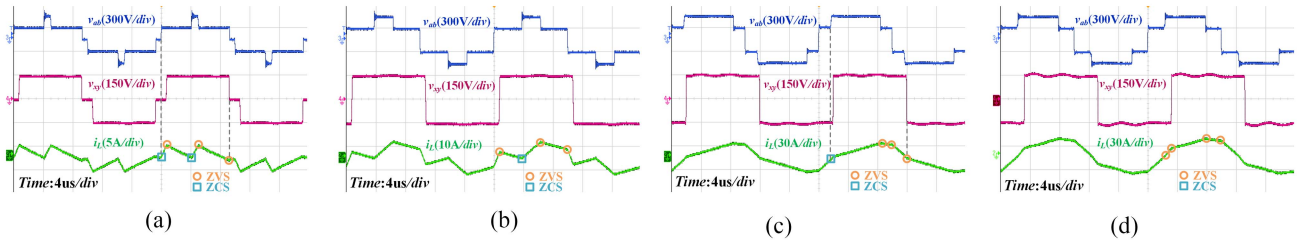

Fig. 10. Typical waveforms during forward power transfer under $V_1 = 300$ V and $V_2 = 150$ V ($k = 1.62$). (a) $P_0 = 0.06$ (under Stage 1). (b) $P_0 = 0.17$ (under Stage 4). (c) $P_0 = 0.56$ (under Stage 5). (d) $P_0 = 0.71$ (under Stage 6).

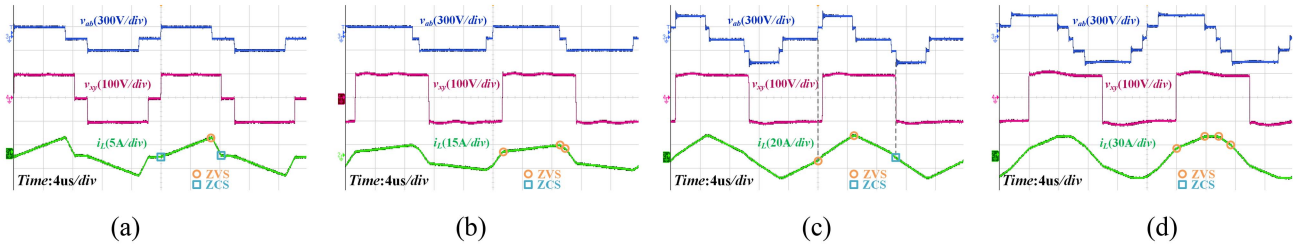

Fig. 11. Typical waveforms during forward power transfer under $V_1 = 300$ V and $V_2 = 100$ V ($k = 2.42$). (a) $P_0 = 0.08$ (under Stage 1). (b) $P_0 = 0.26$ (under Stage 2). (c) $P_0 = 0.51$ (under Stage 3). (d) $P_0 = 0.82$ (under Stage 5).

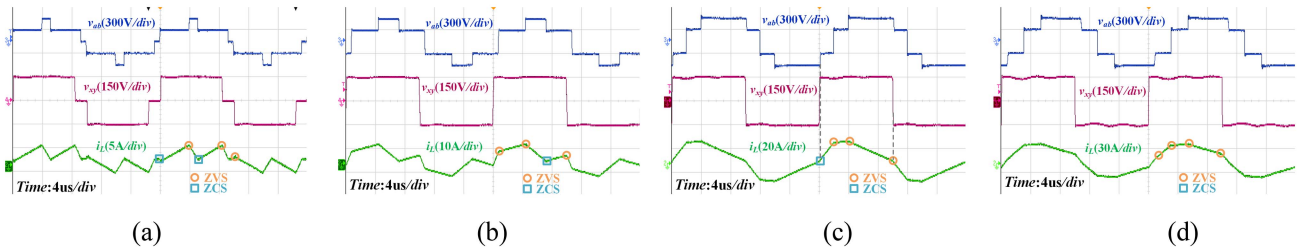

Fig. 12. Typical waveforms during reverse power transfer under $V_1 = 300$ V and $V_2 = 150$ V ($k = 1.62$). (a) $P_0 = 0.06$ (under Stage 1). (b) $P_0 = 0.17$ (under Stage 4). (c) $P_0 = 0.56$ (under Stage 5). (d) $P_0 = 0.71$ (under Stage 6).

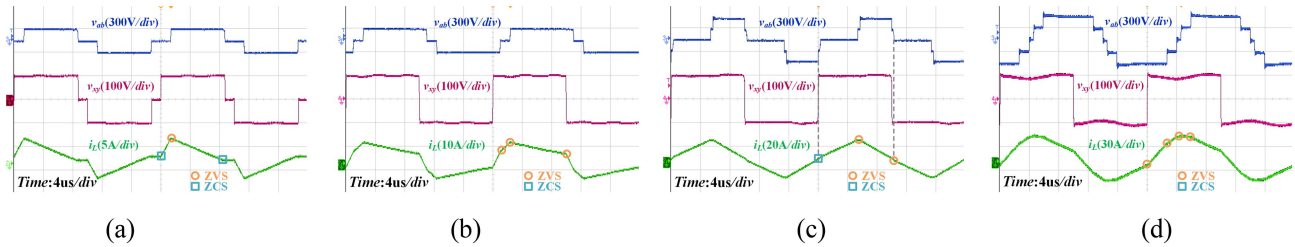

Fig. 13. Typical waveforms during reverse power transfer under $V_1 = 300$ V and $V_2 = 100$ V ($k = 2.42$). (a) $P_0 = 0.08$ (under Stage 1). (b) $P_0 = 0.26$ (under Stage 2). (c) $P_0 = 0.51$ (under Stage 3). (d) $P_0 = 0.82$ (under Stage 5).

without considering ZVS realization. However, at light load, the QPS-MCS modulation exhibits a higher peak current than the proposed OQPS modulation due to inaccurate modeling.

To further verify the effectiveness of the proposed OQPS modulation, various modulations have been implemented in the prototype, with their peak currents and efficiencies measured. The experimental waveforms of various modulations are presented, as shown in Figs. 15 and 16. Also, the peak current and efficiency are labeled in the figure.

The experimental waveforms in Fig. 15 are tested under $V_1 = 300$ V, $V_2 = 150$ V, and $P_0 = 0.17$. It can be found that the peak current under TPS-MCS modulation is maximum at 10.9 A. The peak current under the proposed OQPS modulation is the minimum with 6.6 A. Compared to TPS-MCS modulation and QPS-ZVS modulation, the peak current under the proposed OQPS modulation can be reduced to 61% and 75% of the original. In terms of efficiency, the converter efficiency improves from 94.9% under TPS-MCS modulation to 96.9% under OQPS

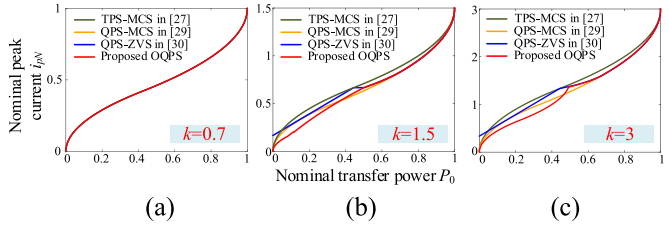

Fig. 14. Nominal peak current of each modulation strategy for variation of the nominal transferred power P_0. (a) When $k = 0.7$. (b) When $k = 1.5$. (c) When $k = 3$.

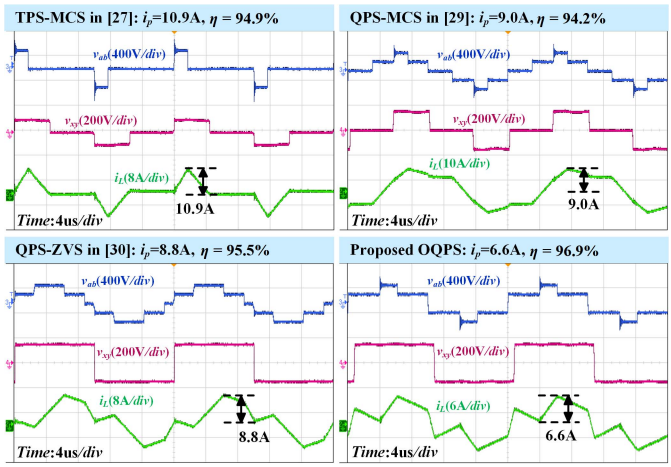

Fig. 15. Experimental waveforms with various modulation strategies under $V_1 = 300$ V, $V_2 = 150$ V, and $P_0 = 0.17$.

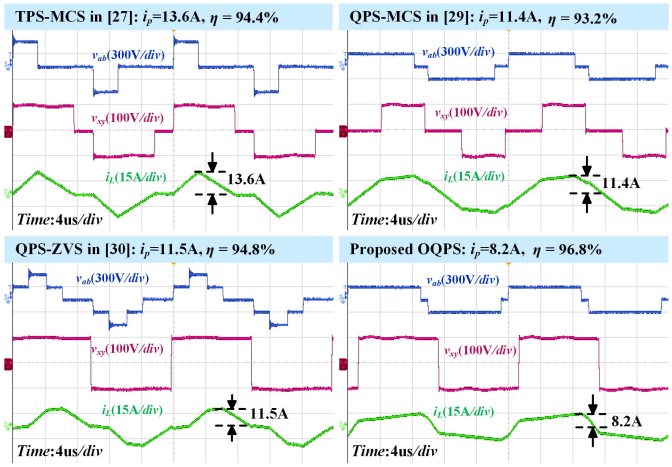

Fig. 16. Experimental waveforms with various modulation strategies under $V_1 = 300$ V, $V_2 = 100$ V, and $P_0 = 0.26$.

modulation. Compared to QPS-ZVS modulation, the efficiency of the converter under OQPS modulation can still be improved by 1.4%.

The experimental waveforms in Fig. 16 are tested under $V_1 = 300$ V, $V_2 = 100$ V, and $P_0 = 0.26$. The same conclusion can be obtained. Among the four modulation strategies, the OQPS modulation has the minimum peak current of 8.2 A. Compared with the TPS-MCS modulation, the peak current of the converter under OQPS modulation can be reduced by 39.7%. Meanwhile,

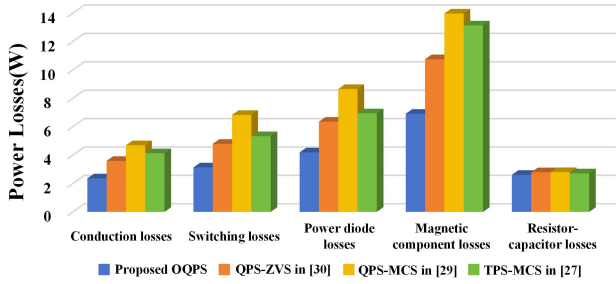

Fig. 17. Comparison of power losses for various modulation strategies under $V_1 = 300$ V, $V_2 = 150$ V, and $P_0 = 0.17$.

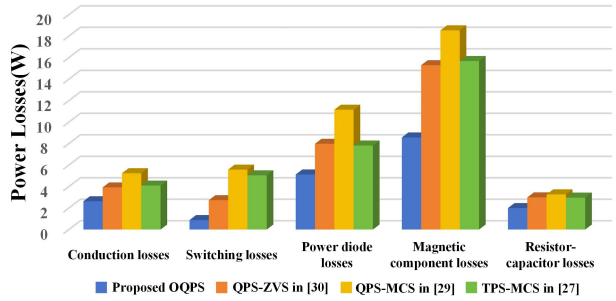

Fig. 18. Comparison of power losses for various modulation strategies under $V_1 = 300$ V, $V_2 = 100$ V, and $P_0 = 0.26$.

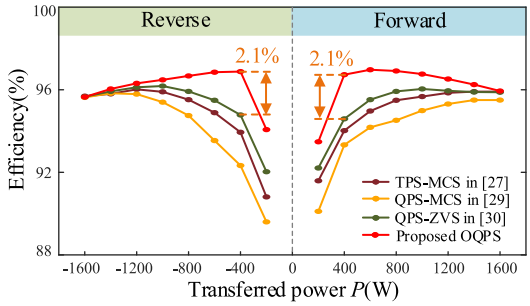

Fig. 19. Efficiency curves for bidirectional power transfer under $V_1 = 300$ V, $V_2 = 150$ V ($k = 1.62$).

the highest efficiency of 96.9% can be achieved under OQPS modulation. Compared to TPS-MCS and QPS-ZVS modulations, the efficiency of the converter is improved by 2.5% and 2.1%, respectively.

Detailed loss distribution and comparison of each modulation under the above two operating conditions are shown in Figs. 17 and 18. The proposed OQPS modulation simultaneously achieves the lowest conduction and switching losses of active switching devices. Among various modulations, the differences in power diode losses and those in magnetic component losses are mainly determined by the current characteristics. Thus, the variation trends of these two types of losses are consistent with those of conduction losses. Resistor–capacitor losses of each modulation are roughly the same but nonnegligible.

When $k < 1$, the optimization results of all four modulation strategies are the same. Therefore, the experimental results for $k < 1$ are not presented.

Figs. 19 and 20 show the efficiency curve for bidirectional power transfer under $V_1 = 300$ V, $V_2 = 150$ V ($k = 1.62$) and

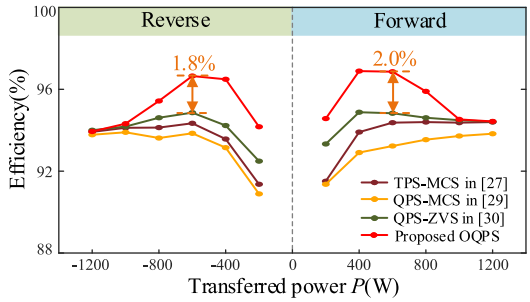

Fig. 20. Efficiency curves with varying transferred power under $V_1 = 300$V, $V_2 = 100$V (k =2.42).

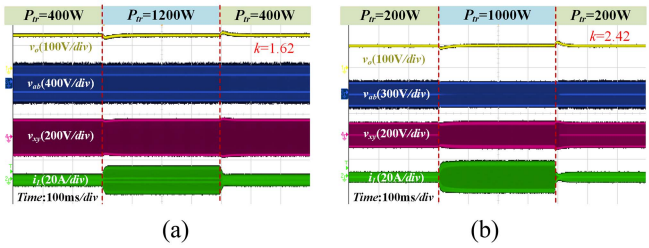

Fig. 21. Dynamic waveforms of the OQPS modulation under closed-loop control. (a) $V_1 = 300$ V, $V_2 = 150$ V (i.e., $k = 1.62$) and P_{tr} changes from 400 to 1200 W and back to 400 W. (b) $V_1 = 300$ V, $V_2 = 100$ V (i.e., $k = 2.42$) and P_{tr} changes from 200 to 1000 W and back to 200 W.

$V_1 = 300$ V, $V_2 = 100$ V ($k = 2.42$), respectively. Among the four optimized modulations, the efficiency of proposed OQPS modulation clearly leads across the entire power range. At $k = 1.62$, compared with QPS-ZVS modulation, the proposed OQPS modulation achieves a 2.1% efficiency improvement at 400-W transferred power. At $k = 2.42$, it achieves a 2.0% efficiency improvement at 600-W transferred power relative to QPS-ZVS modulation. Experimental validation confirms that the proposed OQPS modulation exhibits superior performance in bidirectional power transfer scenarios.

C. Dynamics of the Proposed OQPS Modulation Under Closed-Loop Control

Since the control variables have different analytical expressions in different k-value ranges and power stages, it is crucial to achieve smooth transitions during transferred power variations and k-value variations. Fig. 21 illustrates the dynamics of the proposed OQPS modulation under closed-loop control during load step changes. In Fig. 21(a), the transferred power changes from 400 to 1200 W and back to 400 W under the conditions of $V_1 = 300$ V and $V_2 = 150$ V (i.e., $k = 1.62$). In Fig. 21(b), the transferred power changes from 400 to 1200 W and back to 400 W under the conditions of $V_1 = 300$ V and $V_2 = 100$ V (i.e., $k = 2.42$). It can be seen that the closed-loop control of the proposed OQPS modulation achieves smooth transitions during transferred power variations. To verify the performance of the closed-loop control under k-value variations, Fig. 22 presents the dynamics when the input voltage V_1 switches from 100 to 300 V and vice versa, under the conditions of $V_2 = 100$ V and $P = 600$ W. It can be observed that the closed-loop control of the proposed OQPS modulation still ensures smooth transitions over a wide range of k-value variations.

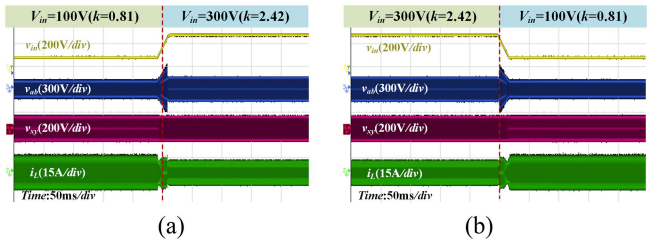

Fig. 22. Dynamic waveforms of the OQPS modulation under the conditions $V_2 = 100$ V and $P = 600$ W. (a) k switches from 0.81 to 2.42. (b) k switches from 2.42 to 0.81.

VII. Conclusion

An OQPS modulation strategy to achieve higher efficiency for the 3/2LNPC-DAB converter is proposed in this article. Conduction losses and switching losses are considered together in the OQPS modulation, aiming to achieve the minimum peak current of the converter under soft switching of all switching devices. First, five operating modes are screened that have the potential to achieve ZVS for all switching devices. Then, the transferred power and peak current expressions for these five modes are derived. Finally, the analytical solution of OQPS modulation is given based on the proposed improved Lagrange function and KKT conditions. Theoretical and experimental results show that the proposed OQPS modulation is able to ensure the minimum peak current under soft switching of all switching devices. Compared to the current state-of-the-art modulation strategy, the proposed OQPS modulation improves the efficiency by 2.1%. Regardless of the variation of k, the proposed OQPS modulation can achieve the highest efficiency in the full power range.

References

[1] P. V. Harisyam and K. Basu, "A single-stage high-frequency-link medium voltage AC to DC converter for utility-scale grid integration of solar and storage," *IEEE Trans. Power Electron.*, vol. 39, no. 12, pp. 15506–15519, Dec. 2024.

[2] R. Pradhan, S. B. Shah, M. I. Hassan, Z. Wang, and A. Emadi, "A 15 kW wide-input reconfigurable three-level DAB converter for on-board charging of 1.25 kV electric vehicle powertrains," *IEEE Trans. Transp. Electrific.*, vol. 10, no. 4, pp. 9144–9162, Dec. 2024.

[3] S. Chaurasiya and B. Singh, "A bidirectional fast EV charger for wide voltage range using three-level DAB based on current and voltage stress optimization," *IEEE Trans. Transp. Electrific.*, vol. 9, no. 1, pp. 1330–1340, Mar. 2023.

[4] S. Shao et al., "Modeling and advanced control of dual-active-bridge DC–DC converters: A review," *IEEE Trans. Power Electron.*, vol. 37, no. 2, pp. 1524–1547, Feb. 2022.

[5] F. Zhang, Y. Ren, X. Yang, W. Chen, and H. Wu, "Capacitor voltage balancing control for a novel 5-level dual active bridge converter," *IEEE Trans. Power Electron.*, vol. 37, no. 12, pp. 14738–14754, Dec. 2022.

[6] J. Wu, D. Liu, Y. Wang, T. Pereira, M. Liserre, and Z. Chen, "Hybrid-bridge-based dual-active-bridge converter with an asymmetric active-neutral-point-clamped three-level bridge," *IEEE Trans. Circuits Syst. I: Reg. Papers*, vol. 71, no. 10, pp. 4873–4886, Oct. 2024.

[7] J. Wu, T. Wang, Z. Shu, L. Ma, S. Wang, and J. Nie, "Power balance control based on sensorless parameters estimation for ISOP three-level DAB converter," *IEEE Trans. Ind. Electron.*, vol. 71, no. 10, pp. 12414–12424, Oct. 2024.

[8] N. Hou, P. Gunawardena, X. Wu, L. Ding, Y. Zhang, and Y. W. Li, "An input-oriented power sharing control scheme with fast-dynamic response for ISOP DAB DC–DC converter," *IEEE Trans. Power Electron.*, vol. 37, no. 6, pp. 6501–6510, Jun. 2022.
[9] Q.-X. Guan, Y. Zhang, H.-B. Zhao, and Y. Kang, "Optimized switching strategy for ANPC–DAB converter through multiple zero states," *IEEE Trans. Power Electron.*, vol. 37, no. 3, pp. 2885–2898, Mar. 2022.
[10] X. Li, X. Zhang, F. Lin, C. Sun, and K. Mao, "Artificial-intelligence-based triple phase shift modulation for dual active bridge converter with minimized current stress," *IEEE J. Emerg. Sel. Top. Power Electron.*, vol. 11, no. 4, pp. 4430–4441, Aug. 2023.
[11] N. Hou and Y. W. Li, "Overview and comparison of modulation and control strategies for a nonresonant single-phase dual-active-bridge DC–DC converter," *IEEE Trans. Power Electron.*, vol. 35, no. 3, pp. 3148–3172, Mar. 2020.
[12] H. Wang, Y. Zeng, S. Ji, Z. Zhao, L. Yuan, and X. Mo, "ZVS soft switching operation region analysis of modular multi active bridge converter under single phase shift control," *IEEE Trans. Ind. Electron.*, vol. 70, no. 7, pp. 6865–6875, Jul. 2023.
[13] T. Chen, R. Yu, A. Q. Huang, and S. Atcitty, "A 480V to 45V GaN bidirectional AC-DC converter for grid-tied battery energy storage system (BESS)," in *Proc. IEEE Appl. Power Electron. Conf. Expo.*, Mar. 2020, pp. 1991–1996.
[14] L. Deng, G. Zhou, Q. Bi, and N. Xu, "Online reactive power minimization and soft switching algorithm for triple-phase-shift modulated dual active bridge converter," *IEEE Trans. Ind. Electron.*, vol. 70, no. 3, pp. 2543–2555, Mar. 2023.
[15] A. K. Bhattacharjee and I. Batarseh, "Optimum hybrid modulation for improvement of efficiency over wide operating range for triple-phase-shift dual-active-bridge converter," *IEEE Trans. Power Electron.*, vol. 35, no. 5, pp. 4804–4818, May 2020.
[16] G. Yang, A. Wang, and D. Zhang, "Transient DC bias suppression for three-level dual active bridge converter," *IEEE Trans. Power Electron.*, vol. 40, no. 9, pp. 12084–12094, Sep. 2025.
[17] C. Song, N. Wang, A. Sangwongwanich, Y. Yang, and F. Blaabjerg, "Evaluation of capacitor voltage balancing control strategies for multilevel DAB converters," *IEEE Trans. Power Electron.*, vol. 39, no. 12, pp. 15548–15564, Dec. 2024.
[18] A. Filba-Martinez, S. Busquets-Monge, J. Nicolas-Apruzzese, and J. Bordonau, "Operating principle and performance optimization of a three-level NPC dual-active-bridge DC–DC converter," *IEEE Trans. Ind. Electron.*, vol. 63, no. 2, pp. 678–690, Feb. 2016.
[19] A. Tong, L. Hang, G. Li, X. Jiang, and S. Gao, "Modeling and analysis of a dual-active-bridge-isolated bidirectional DC/DC converter to minimize RMS current with whole operating range," *IEEE Trans. Power Electron.*, vol. 33, no. 6, pp. 5302–5316, Jun. 2018.
[20] P. Yang, M. Wang, S. Liu, S. Li, X. Chen, and Y. Peng, "Unilateral asymmetric triple phase shift modulation strategy for DAB converter compromising RMS current and soft-switching range," *IEEE Trans. Circuits Syst. II: Exp. Briefs*, vol. 71, no. 6, pp. 3216–3220, Jun. 2024.
[21] Z. Zhang et al., "Optimized modulation strategy of NH3L-DAB converter to minimize RMS current for wide voltage range applications," *IEEE Trans. Power Electron.*, vol. 37, no. 7, pp. 7789–7808, Jul. 2022.
[22] D. Mou et al., "Modeling and analysis of hybrid dual active bridge converter to optimize efficiency over whole operating range," *IEEE J. Emerg. Sel. Top. Power Electron.*, vol. 11, no. 1, pp. 432–441, Feb. 2023.
[23] L. D. James, C. A. Teixeira, R. H. Wilkinson, B. P. McGrath, D. G. Holmes, and J. Riedel, "Adaptive modulation of resonant DAB converters for wide range ZVS operation with minimum reactive circulating power," *IEEE Trans. Ind. Appl.*, vol. 58, no. 6, pp. 7396–7407, Nov./Dec. 2022.
[24] P. Liu, C. Chen, and S. Duan, "An optimized modulation strategy for the three-level DAB converter with five control degrees of freedom," *IEEE Trans. Ind. Electron.*, vol. 67, no. 1, pp. 254–264, Jan. 2020.
[25] Y. Wang et al., "Minimum-current-stress scheme of three-level dual-active-bridge DC–DC converters with the particle swarm optimization," *IEEE Trans. Transp. Electrific.*, vol. 7, no. 4, pp. 2067–2084, Dec. 2021.
[26] J. Tian, C. Zhuo, F. Wang, and H. Deng, "An RMS current minimization method for three-level ANPC-DAB-based distributed energy storage system with full operation ZVS," *IEEE J. Emerg. Sel. Top. Power Electron.*, vol. 12, no. 3, pp. 2388–2405, Jun. 2024.
[27] S. Shao, M. Jiang, W. Ye, Y. Li, J. Zhang, and K. Sheng, "Optimal phase-shift control to minimize reactive power for a dual active bridge DC–DC converter," *IEEE Trans. Power Electron.*, vol. 34, no. 10, pp. 10193–10205, Oct. 2019.
[28] J. Yang et al., "Online digital implementation of wide voltage range RMS-current-optimized control with voltage balancing capability for DAB converter," *IEEE Trans. Power Electron.*, vol. 38, no. 4, pp. 4360–4377, Apr. 2023.
[29] C. Song, A. Sangwongwanich, Y. Yang, Y. Pan, and F. Blaabjerg, "Analysis and optimal modulation for 2/3-level DAB converters to minimize current stress with five-level control," *IEEE Trans. Power Electron.*, vol. 38, no. 4, pp. 4596–4612, Apr. 2023.
[30] C. Song, A. Sangwongwanich, Y. Yang, and F. Blaabjerg, "Optimal control of multilevel DAB converters for soft-switching and minimum current stress," *IEEE Trans. Power Electron.*, vol. 39, no. 5, pp. 5707–5720, May 2024.
[31] B. Zhao, Q. Song, W. Liu, G. Liu, and Y. Zhao, "Universal high-frequency-link characterization and practical fundamental-optimal strategy for dual-active-bridge DC-DC converter under PWM plus phase-shift control," *IEEE Trans. Power Electron.*, vol. 30, no. 12, pp. 6488–6494, Dec. 2015.
[32] Z. Wang, C. Li, J. Liu, and Z. Zheng, "Influence of junction-capacitance and dead-time on dual-active-bridge actual soft-switching-range: Analytic analysis and solution," *IEEE Trans. Power Electron.*, vol. 38, no. 5, pp. 6157–6168, May 2023.
[33] M. Kasper, R. Burkat, F. Deboy, and J. Kolar, "ZVS of power MOSFETs revisited," *IEEE Trans. Power Electron.*, vol. 31, no. 12, pp. 8063–8067, Dec. 2016.
[34] Z. Feng, H. Wen, X. Han, G. Wang, Y. Zhu, and J. Rodrigues, "A deep reinforcement learning framework for 3L-NPC-DAB converters with multiple-degree-of-freedom phase-shift control," *IEEE Trans. Transp. Electrific.*, vol. 11, no. 4, pp. 9346–9358, Aug. 2025.
[35] J. Muhlethaler, J. Biela, J. W. Kolar, and A. Ecklebe, "Core losses under the DC bias condition based on Steinmetz parameters," *IEEE Trans. Power Electron.*, vol. 27, no. 2, pp. 953–963, Feb. 2012.
[36] F. Tourkhani and P. Viarouge, "Accurate analytical model of winding losses in round Litz wire windings," *IEEE Trans. Magn.*, vol. 37, no. 1, pp. 538–543, Jan. 2001.

Jiayun Liu was born in Hunan, China, in 2001. He received the B.S. degree in electrical engineering in 2022 from Hunan University, Changsha, China, where he is currently working toward the Ph.D. degree in electrical engineering.

His research interests include multilevel converters, soft-switching power converters, and isolated bidirectional ac–dc converters.

Cheng Tang was born in Hunan, China, in 1996. He received the B.S. degree in electrical engineering and automation and the Ph.D. degree in electrical engineering from Hunan University, Changsha, China, in 2019 and 2024, respectively.

He is currently a Postdoctoral Fellow with the College of Electrical and Information Engineering, Hunan University. His research interests include power conversion control, active thermal control, and model-predictive control.

Jiayu Hu was born in Jilin, China, in 1996. He received the B.S. degree in 2018 and the Ph.D. degree in 2023 from the College of Electrical and Information Engineering, Hunan University, Changsha, China, both in electrical engineering.

He is currently a Senior Hardware Engineer with Sungrow Power Supply Company, Hefei, China. His primary research interests include switching power amplifiers, soft-switching power converters, solid-state transformers, and their applications within the field of power electronics.

Qianming Xu (Member, IEEE) was born in Henan, China, in 1989. He received the B.S. degree in electrical engineering and automation and the Ph.D. degree in electrical engineering from Hunan University, Changsha, China, in 2012 and 2017, respectively.

Since 2023, he has been a Professor with the College of Electrical and Information Engineering, Hunan University. His research interests include multilevel converter, power electronic reliability monitoring, and power quality control.

Peng Guo (Member, IEEE) was born in Hunan, China, in 1992. He received the B.S. degree in electrical engineering from the Wuhan University of Technology, Wuhan, China, in 2015, and the Ph.D. degree in electrical engineering from Hunan University, Changsha, China, in 2020.

From 2020 to 2023, he was a Postdoctoral Fellow with Hunan University, where he is currently an Associate Professor with the College of Electrical and Information Engineering. His research interests include switch-mode power amplifier, data-driven nonlinear control, electromagnetic sensing, and electromagnetic compatibility for high-frequency power electronics systems.

Guanqing Zhou received the B.S. and M.S. degrees in electrical engineering from the Hefei University of Technology, Hefei, China, in 2019 and 2022, respectively. He is currently working toward the Ph.D. degree with the School of Electrical and Information Engineering, Hunan University, Changsha, China.

His research interests include high-frequency link power conversion systems and isolated bidirectional ac–dc converters.

Xiangpeng Liu was born in Hubei, China, in 2001. He received the B.S. degree in electrical engineering from Chongqing University, Chongqing, China, in 2023. He is currently working toward the M.S. degree in electrical engineering with the College of Electrical and Information Engineering, Hunan University, Changsha.

His main research interests include high-frequency link inverter and isolated bidirectional ac–dc converters.

Zhikang Shuai (Senior Member, IEEE) received the B.S. and Ph.D. degrees from the College of Electrical and Information Engineering, Hunan University, Changsha, China, in 2005 and 2011, respectively, all in electrical engineering.

From 2009 to 2012, he was an Assistant Professor with Hunan University, where he became an Associate Professor in 2013 and a Professor in 2014. His research interests include power quality control, power electronics, and microgrid stability analysis and control.

Dr. Shuai is the recipient of the 2010 National Scientific and Technological Awards of China, the 2012 Hunan Technological Invention Awards of China, and the 2007 Scientific and Technological Awards from the National Mechanical Industry Association of China. He is an Associate Editor for *CSEE Journal of Power and Energy Systems* and *Chinese Journal of Electrical Engineering*.